

# Incorporating waveform calibration error in gravitational-wave modeling and inference for SEOBNRv4

Ritesh Bachhar,<sup>1,\*</sup> Michael Pürrer,<sup>1,2</sup> and Stephen R. Green<sup>3,2</sup>

<sup>1</sup>*Department of Physics and Center for Computational Research, East Hall, University of Rhode Island, Kingston, RI 02881*

<sup>2</sup>*Max Planck Institute for Gravitational Physics (Albert Einstein Institute), Am Mühlenberg 1, Potsdam 14476, Germany*

<sup>3</sup>*School of Mathematical Sciences, University of Nottingham,  
University Park, Nottingham NG7 2RD, United Kingdom*

(Dated: October 23, 2024)

As gravitational wave (GW) detector networks continue to improve in sensitivity, the demand on the accuracy of waveform models which predict the GW signals from compact binary coalescences is becoming more stringent. At high signal-to-noise ratios (SNRs) discrepancies between waveform models and the true solutions of Einstein's equations can introduce significant systematic biases in parameter estimation (PE). These biases affect the inferred astrophysical properties, including matter effects, and can also lead to erroneous claims of deviations from general relativity, impacting the interpretation of astrophysical populations and cosmological parameters. While efforts to address these biases have focused on developing more precise models, we explore an alternative strategy to account for uncertainties in waveform models, particularly from calibrating an effective-one-body (EOB) model against numerical relativity (NR) data. We introduce an efficient method for modeling and marginalizing over waveform uncertainty in the SEOBNRv4 model, which captures the dominant (2, 2) mode for non-precessing quasi-circular binary black holes (BBHs). Our approach uses Gaussian process regression (GPR) to model amplitude and phase deviations in the Fourier domain. This method mitigates systematic biases in PE and increases posterior variance by incorporating a broader distribution of waveforms, consistent with previous findings. This study emphasizes the importance of incorporating waveform uncertainties in GW data analysis and presents a novel, practical framework to include these uncertainties in Bayesian PE for EOB models, with broad applicability.

## I. INTRODUCTION

To date approximately 100 GW signals from the coalescence of compact binaries have been observed by the LIGO-Virgo-KAGRA (LVK) collaboration [1–5]. Accurate waveform models are essential for robust estimation of source parameters [6–10]. However, these models are in practice subject to systematic uncertainties. Inspiral-merger-ringdown waveform models are in general constructed from an approximate ansatz which is tuned to a finite set of NR simulation data [6]. Internally, approximate fits against NR data are used to predict model coefficients over the binary parameter space. We refer to errors arising at each NR point and in the fits over parameter space as *waveform calibration errors*. This is the case for the phenomenological [11–23] and EOB models [24–35] in use today. In contrast, NR surrogates model a set of NR simulation data directly in a data driven way, with imperfections arising from errors in reduced bases and fits over parameter space and have been shown to be highly accurate [36–41].

GW catalogs have so far used techniques where posterior samples for different GW models are combined with equal weights [4], weighted by their respective evidences [42], or by averaging the likelihood [43]. Alternatively, one can sample a set of models in a single joint

Bayesian analysis [44, 45], and prioritize the most accurate model in each region of parameter space [46]. In this study, we incorporate waveform calibration uncertainties into Bayesian inference for the SEOBNRv4 model, focusing on improving the accuracy (and reduce bias) of parameter estimates at the expense of precision (expecting wider posterior distributions).

As GW detectors are becoming more sensitive the rate of events is ever increasing, as well as the SNR for golden events. Waveform systematics arise when there are discrepancies between a particular waveform model and the true GW signal from solving Einstein's equations, assuming that general relativity (GR) is the correct theory of gravity. These errors can significantly impact the posterior distributions of the inferred source parameters, leading to biased results [47–53]. The motivation for this work is rooted in the need to refine posterior distributions of approximate waveform models for moderate to high SNR events where waveform systematics will arise. One way to reduce biases is to increase the accuracy of waveform models. This requires improvements in approximation theory, waveform construction, and most importantly, an extensive set of NR simulations covering the the high dimensional binary parameter space, a requirement which is strongly computationally limited. Here we follow an alternative approach by including uncertainties inherent in an existing model itself. We adopt a novel approach using Gaussian process regression to interpolate amplitude and phase differences between the calibrated SEOBNRv4 model and an uncalibrated version of this EOB model

---

\* [riteshbachhar@uri.edu](mailto:riteshbachhar@uri.edu)

where calibration parameters are sampled from calibration posterior distributions at points in parameter space where NR waveforms are available. A calibration posterior arises from a likelihood function which encodes discrepancies between the uncalibrated EOB model and an NR simulation. This approach enables the transition from a deterministic to a probabilistic waveform model, effectively capturing the model uncertainty.

The idea of marginalizing over waveform uncertainty in parameter estimation was first proposed by Moore & Gair [54, 55] in an idealized setting. Their approach is elegant and relies on the approximation of the strain difference by a Gaussian process which allows for analytical marginalization in a likelihood function which is marginalized over waveform uncertainty. For the sake of efficiency, and because strain differences are difficult to model directly, we instead apply a frequency-dependent amplitude and phase error to each template waveform which enters the GW likelihood function. This methodology is inspired by established techniques for marginalizing over detector calibration uncertainty [56, 57] and applications of this parametrization. In particular, Edelman *et al.* [58] augmented an existing waveform model with spline parametrized amplitude and phase deviations in the Fourier domain to constrain unmodeled physics, while Read [59] used a similar ansatz to quantify the amplitude and phase accuracy of waveform models for neutron star inspirals. In a similar spirit Owen *et al.* [60] employed a post-Newtonian (PN)-based method to mitigate waveform systematics has recently been introduced by where the authors propose to marginalize over higher order PN coefficients.

Several studies have investigated the use of probabilistic waveform models. For instance, a GPR model based on spin-aligned phenomenological waveforms was built by [61] along with a greedy method for predicting where new training waveforms should be placed to reduce modeling error. Additionally, [62] trained a model on precessing NR simulations using a Gaussian process (GP) which is joint in model parameters and time. A combination of active learning with GPR was explored in [63] to train an EOB model against NR data. More recently, GPR was employed to developing a probabilistic extension to the phenomenological modeling workflow for non-spinning black holes (BHs) while taking into account the estimated numerical error in NR simulations.

This study is similar to the one discussed in Pompili *et al.* [64]. Both studies introduce a method for modeling waveform uncertainty arising in the calibration of EOB models against NR data and use these models in a Bayesian inference study. While the overall goals align strongly, there are significant differences in how the uncertainty models are constructed and how uncertainty is incorporated into PE.

The stochasticity in our uncertainty model arises from a multivariate normal approximation of the distribution of amplitude and phase differences at points in parameter space where NR simulations were available at the time of

construction of the SEOBNRv4 model. Subsequently, we use GPR to interpolate the means and covariance matrices of amplitude and phase deviations over parameter space.

By integrating waveform calibration errors into the SEOBNRv4 model we explore additional variations in the waveform templates, with the aim of improving the accuracy of GW parameter estimates at the expense of precision. While our method is presented for a particular EOB model, it is broadly applicable for any waveform model where a distribution of waveforms around the best fit waveform is available at calibration points over the binary parameter space. This approach not only provides a comprehensive uncertainty quantification but also paves the way for more robust tests of general relativity and enhanced astrophysical inferences.

This paper is organized as follows. In Sec. II we present a comprehensive summary of methods pertaining to the comparison of waveforms, we discuss GPR and its use in analytic marginalization over waveform uncertainty, and summarize the SEOBNRv4 model. We go on to discuss the construction of our new uncertainty model, as well as an introduction to Bayesian PE. In Sec. III we present setup and results of our PE study which compares posterior distributions obtained with a number of aligned-spin (2, 2) mode models, including our uncertainty model on a set of NR surrogate signals over parameter space. Lastly, we summarize our results and conclusions in Sec. IV.

## II. METHODOLOGY

In this section we discuss metrics for comparing waveforms in Sec. II A, summarize Gaussian process regression in Sec. II B, and how Gaussian processes can be used to define a likelihood function which marginalizes over waveform uncertainty in Sec. II C. We discuss the calibration of the SEOBNRv4 waveform model against NR simulations in Sec. II D, and the construction of an SEOBNRv4-based model which includes waveform uncertainty in Sec. II E. Finally, we introduce Bayesian parameter estimation for compact binary coalescences in Sec. II F.

### A. Waveform metrics and parameters

A GW signal emitted by an aligned-spin quasi-circular BBH observed in the detector frame depends on the component masses  $m_1, m_2$ , dimensionless spins  $\chi_i = \hat{L} \cdot S_i / m_i^2$  for BHs  $i = 1, 2$  where  $\hat{L}$  is the angular orbital momentum unit vector, the time  $t_c$  and phase  $\phi_c$  of coalescence, the inclination angle  $\iota$  of the source as seen by the observer, the luminosity distance  $d_L$  and sky location (ra, dec) of the source and the polarization angle  $\psi$ . Instead of the component masses, we use the chirp mass  $\mathcal{M} = M\eta^{3/5}$  and (asymmetric) mass-ratio  $q = m_1/m_2 \geq 1$ , where  $M = m_1 + m_2$  is the total mass, and  $\eta = q/(1+q)^2$  is the symmetric mass-ratio. We use the effective aligned spin parameter  $\chi_{\text{eff}} = (m_1\chi_1 + m_2\chi_2)/M$ .

We decompose a gravitational waveform  $h(t)$  into modes in a basis of spherical harmonics of spin weight -2,

$$h_+(t) - ih_\times(t) = \sum_{\ell, m} -2Y_{\ell m}(t)h_{\ell m}(\theta, \phi). \quad (1)$$

The *overlap* between two waveforms  $h_1$  and  $h_2$  can be defined as

$$\mathcal{O}(h_1, h_2) := \frac{\langle h_1 | h_2 \rangle}{\sqrt{\langle h_1 | h_1 \rangle \langle h_2 | h_2 \rangle}}, \quad (2)$$

where the noise-weighted inner product is given by

$$\langle h_1 | h_2 \rangle = 4\text{Re} \int_{f_{\text{low}}}^{f_{\text{high}}} \frac{\tilde{h}_1(f)\tilde{h}_2^*(f)}{S_n(f)} df \quad (3)$$

where  $\tilde{\cdot}$  denotes the Fourier transform,  $S_n$  is the one-sided power spectral density (PSD) of the noise, and  $*$  denotes complex conjugation.

We define the *match* as the overlap maximized over time and phase-shifts between the two waveforms

$$\mathfrak{M}(h_1, h_2) := \max_{t_c, \phi_c} \mathcal{O}(h_1, h_2), \quad (4)$$

and the *mismatch* as  $\bar{\mathfrak{M}}(h_1, h_2) = 1 - \mathfrak{M}(h_1, h_2)$ .

The (optimal) signal-to-noise ratio (SNR) in a single GW detector is defined as

$$\rho = \sqrt{\langle h | h \rangle}. \quad (5)$$

For a multi-detector network the SNR adds in quadrature, defining the network SNR, a useful measure of how loud a GW signal is.

## B. Gaussian process regression

GPR[65, 66] is a (nonparametric) probabilistic interpolation algorithm. It starts from a set of training data which we assume to be pairs of intrinsic parameters  $\vec{\lambda}_i$  and a waveform difference  $\delta h$

$$\mathcal{D} = \left\{ \left( \vec{\lambda}_i, \delta h(\vec{\lambda}_i) \right) \right\}_{i=1}^n. \quad (6)$$

(Later we will use amplitude and phase differences instead of waveform differences.)

We assume that all waveform differences in  $\mathcal{D}$  are drawn from a multi-variate Gaussian distribution and are modeled by a GP with zero mean and *covariance function*  $k(\cdot, \cdot)$ . Then, it can be shown that the joint distribution of all waveform differences in the training set and the waveform difference at a new point  $\vec{\lambda} \notin \mathcal{D}$  is still multi-variate Gaussian

$$P \left( \begin{bmatrix} \delta h(\vec{\lambda}_1) \\ \vdots \\ \delta h(\vec{\lambda}_n) \\ \delta h(\vec{\lambda}) \end{bmatrix} \right) \sim \mathcal{N}(\mathbf{0}, \mathbf{M}) \quad (7)$$

with covariance matrix

$$\mathbf{M} = \begin{pmatrix} \mathbf{K} & \mathbf{K}_* \\ \mathbf{K}_*^T & K_{**} \end{pmatrix}, \quad (8)$$

where the sub-matrices are given in terms of the covariance function

$$(\mathbf{K})_{ij} = k(\vec{\lambda}_i, \vec{\lambda}_j), \quad (\mathbf{K}_*)_i = k(\vec{\lambda}_i, \vec{\lambda}), \quad K_{**} = k(\vec{\lambda}, \vec{\lambda}). \quad (9)$$

For a stationary and smooth GP the covariance function can be chosen as

$$k(\vec{\lambda}_i, \vec{\lambda}_j) = \sigma_f^2 \exp \left[ -\frac{1}{2} g_{ab} (\vec{\lambda}_i - \vec{\lambda}_j)^a (\vec{\lambda}_i - \vec{\lambda}_j)^b \right] + \sigma_n^2 \delta_{ij}, \quad (10)$$

with  $g_{ab} = \text{const}$ , where  $\sigma_f$  and  $\sigma_n$  are scale factors. We take  $g_{ab}$  to be diagonal.

To train a GP we can maximize the hyper-likelihood (or evidence for  $\mathcal{D}$ )

$$\log Z(\theta | \mathcal{D}) = -\frac{1}{2} (\mathbf{K}^{-1})_{ij} \langle \delta h(\vec{\lambda}_i) | \delta h(\vec{\lambda}_j) \rangle - \frac{1}{2} \log |\mathbf{K}| \quad (11)$$

over hyper-parameters  $\theta = (\sigma_f, g_{ab}, \sigma_n)$  to find

$$\hat{\theta} = \underset{\hat{\theta}}{\text{argmax}} Z(\hat{\theta} | \mathcal{D}). \quad (12)$$

Having determined  $k(\cdot, \cdot)$  at  $\hat{\theta} = (\hat{\sigma}_f, \hat{g}_{ab})$  one can show that

$$P(\delta h(\vec{\lambda}) | \mathcal{D}) \propto \exp \left[ -\frac{\|\delta h(\vec{\lambda}) - \mu(\vec{\lambda})\|^2}{2\sigma^2(\vec{\lambda})} \right] \quad (13)$$

where

$$\mu(\vec{\lambda}) = (\mathbf{K}_*)_i (\mathbf{K}^{-1})_{ij} \delta h(\vec{\lambda}_j) \quad (14)$$

$$\sigma^2(\vec{\lambda}) = K_{**} - (\mathbf{K}_*)_i (\mathbf{K}^{-1})_{ij} (\mathbf{K}_*)_j. \quad (15)$$

## C. Analytic marginalization over waveform uncertainty

We briefly summarize the ideas of Moore & Gair [54, 55]. The basic idea is to construct a prior probability distribution on the waveform difference  $\delta h(\vec{\lambda}) = H(\vec{\lambda}) - h(\vec{\lambda})$ , where  $H(\vec{\lambda})$  is taken to be an approximate and  $h(\vec{\lambda})$  an accurate waveform model (e.g. NR).

The standard likelihood function assuming stationary Gaussian noise for the accurate model is

$$L'(s | \vec{\lambda}) \propto \exp \left[ -\frac{1}{2} \|s - h(\vec{\lambda})\|^2 \right], \quad (16)$$

but in practice we only have access to the approximate model over parameter space with likelihood

$$L(s | \vec{\lambda}) \propto \exp \left[ -\frac{1}{2} \|s - H(\vec{\lambda})\|^2 \right] \approx L'. \quad (17)$$

One can then define a likelihood which accounts for uncertainty in  $H(\vec{\lambda})$

$$\mathcal{L}(s|\vec{\lambda}) \propto \int d(\delta h(\vec{\lambda})) P(\delta h(\vec{\lambda})) \exp\left[-\frac{1}{2}\|s - H(\vec{\lambda}) + \delta h(\vec{\lambda})\|^2\right]. \quad (18)$$

We will assume that  $\delta h(\vec{\lambda})$  is the realization of a GP. A GP furnishes a conditional probability distribution given training data  $\mathcal{D}$

$$\delta h(\vec{\lambda}) \sim \mathcal{GP}(m(\vec{\lambda}) = 0, k(\vec{\lambda}, \vec{\lambda}')) \quad (19)$$

or

$$P(\delta h(\vec{\lambda})|\mathcal{D}) \propto \exp\left[-\frac{\|\delta h(\vec{\lambda}) - \mu(\vec{\lambda})\|^2}{2\sigma^2(\vec{\lambda})}\right], \quad (20)$$

where

$$\mathcal{D} = \left\{ \left( \vec{\lambda}_i, \delta h(\vec{\lambda}_i) \right) \right\}_{i=1}^n. \quad (21)$$

Therefore, the likelihood marginalized over waveform uncertainty is a convolution of two Gaussians

$$\mathcal{L}(s|\vec{\lambda}) \propto \frac{1}{1 + \sigma^2(\vec{\lambda})} \exp\left[-\frac{1}{2} \frac{\|s - H(\vec{\lambda}) + \mu(\vec{\lambda})\|^2}{1 + \sigma^2(\vec{\lambda})}\right]. \quad (22)$$

Comparing Eq.(22) with the likelihood for the approximate model Eq. (17) we see that the mean has been shifted by  $\mu(\vec{\lambda})$  and the variance has increased by  $\sigma^2(\vec{\lambda})$ .

#### D. The SEOBNRv4 waveform model

SEOBNRv4 [24] models quasi-circular non-precessing aligned-spin BBHs in the effective-one-body EOB formalism. The binary dynamics for the inspiral and plunge is determined by an EOB Hamiltonian and a radiation reaction force. The final GW waveform combines inspiral-plunge and merger-ringdown parts of the (2,2) mode. It depends on four calibration parameters which are then tuned to data from a set of NR simulations.

The uncalibrated SEOBNRv4 model  $h_{\text{EOB}}(\lambda, \theta)$  depends on two sets of parameters: (i) three intrinsic physical parameters  $\lambda = (q, \chi_1, \chi_2)$ , and (ii) four *calibration parameters*  $\theta = (K, d_{SO}, d_{SS}, \Delta t_{\text{peak}}^{22})$ . The calibration parameters enter into the inspiral-plunge part of the EOB waveform.  $K$  determines the position of the EOB horizon and the shape of the radial potential in the strong-field region,  $d_{SO}$  and  $d_{SS}$  are spin-orbit and spin-spin parameters which enter the EOB spin mapping, and  $\Delta t_{\text{peak}}^{22}$  is the difference between the peak of orbital frequency and the peak of radiation in time. Of course the model also depends on additional physical parameters listed in Sec. II A in a straightforward manner; here we single out

$\lambda$  because this is the subset of physical parameters over which BBH NR simulations vary.

Calibration against NR simulations fixes a mapping  $\theta(\lambda)$  based on the match between EOB waveforms and NR at 141 specific points  $\{\lambda_i\}$  in parameter space (see App. C of Ref. [24] for the list of included NR simulations, and Fig. 1 of Ref. [24] for a graphical representation of their distribution). The point of calibration is to increase the accuracy of the EOB model when compared to independent NR simulations. An accuracy measure can be defined as the mismatch

$$\overline{\mathfrak{M}}(\theta) = \overline{\mathfrak{M}}(h_{\text{EOB}}(\lambda; \theta), h_{\text{NR}}(\lambda)) \quad (23)$$

but the authors of [24] also found it beneficial to include a term  $\delta t_{\text{peak}}^{22}(\theta)$  for the merger time difference between EOB and NR, after phase alignment. Given its definition,  $\Delta t_{\text{peak}}^{22}$  affects the EOB merger time, and therefore  $\delta t_{\text{peak}}^{22}(\theta)$ . The mismatch and merger time difference are combined in the definition of a Gaussian likelihood function

$$p(\lambda_i|\theta) \propto \exp\left[-\frac{1}{2} \left(\frac{\overline{\mathfrak{M}}_{\text{max}}(\theta)}{\sigma_{\mathfrak{M}}}\right)^2 - \frac{1}{2} \left(\frac{\delta t_{\text{peak}}^{22}(\theta)}{\sigma_t}\right)^2\right], \quad (24)$$

where  $\overline{\mathfrak{M}}_{\text{max}}(\theta)$  is the maximum mismatch over total masses between 10 and  $200M_{\odot}$ . The standard deviations are chosen as  $\sigma_{\mathfrak{M}} = 0.01$  and  $\sigma_t = 5M$ .

The calibration procedure involves the following steps: (i) For each  $\lambda_i$  determine the *calibration posterior* distribution  $p(\theta|\lambda_i)$  assuming a flat prior in  $\theta$  using an MCMC sampler. See Fig. 1 for an example. (ii) Discard calibration posterior samples with  $\overline{\mathfrak{M}}_{\text{max}} > 1\%$  and  $|\delta t_{\text{peak}}^{22}| > 5M$ . (iii) Remove secondary modes from the posteriors  $p(\theta|\lambda_i)$

Finally, a polynomial fit is performed to the means of the calibration posteriors  $\bar{\theta}(\lambda_i)$  to obtain a mapping  $\theta(\lambda)$  throughout physical parameter space as discussed in Ref. [24]. With this prescription it was found that the maximum mismatch of the resulting calibrated SEOBNRv4 model against the available NR waveforms was less than 1%. Detailed mismatch comparisons against NR are shown in [24].

#### E. Model for waveform uncertainty in SEOBNRv4

We introduce a novel method to build an effective-one-body model which includes waveform uncertainty based on posterior distributions of EOB calibration parameters given a set of NR simulations. This allows us to replace a usual deterministic waveform model  $h(\lambda)$  with a probabilistic waveform model  $p(h|\lambda)$ . Our method uses a computationally efficient ansatz in terms of amplitude and phase deviations. These deviations are computed between the calibrated SEOBNRv4 model and samples from

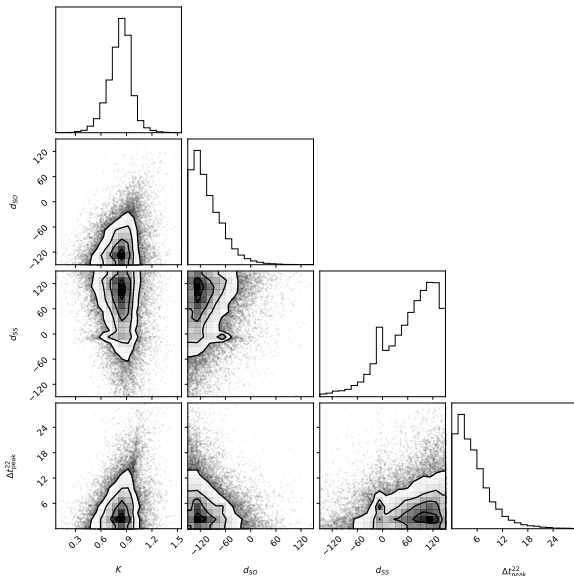


Figure 1. A corner plot of an example calibration posterior distribution  $p(\theta|\lambda_i)$  for an SXS simulation at  $q = 2$ ,  $\chi_1 = 0$ ,  $\chi_2 = -0.6$ .

an uncalibrated SEOBNRv4 conditioned on calibration posteriors. We first determine the distribution of deviations at each NR calibration point  $\lambda$ , and subsequently interpolate the distributions over the binary parameter space.

### 1. Construction of calibration error model

We make the following ansatz for the calibration error (CE) model to achieve a compressed frequency domain representation of the waveform uncertainty arising in calibration of SEOBNRv4 (here abbreviated as “EOB”) against NR simulations:

$$\tilde{h}_{\text{CE}}(\lambda; f) = [1 + \delta A(\lambda; f)] e^{i\delta\phi(\lambda; f)} \times \tilde{h}_{\text{EOB}}(\lambda; f), \quad (25)$$

where  $\delta A$  and  $\delta\phi$  are relative amplitude and absolute phase deviations. Expanding  $\tilde{h}_{\text{EOB}} = A_{\text{EOB}} e^{i\phi_{\text{EOB}}}$  the deviations can be computed as

$$\delta A(f) = A_{\text{CE}}(f)/A_{\text{EOB}}(f) - 1 \quad (26)$$

$$\delta\phi(f) = \phi_{\text{CE}}(f) - \phi_{\text{EOB}}(f). \quad (27)$$

At each NR calibration point  $\lambda_i$  we compute the distribution of deviations

$$p((\delta A, \delta\phi)|\lambda_i) \quad (28)$$

given the uncalibrated SEOBNRv4 model  $h_{\text{EOB}}(\lambda, \theta)$  and calibration posterior samples  $\theta_k \sim p(\theta|h_{\text{NR}}(\lambda_i))$ . I.e. we set  $A_{\text{CE}}^{i,k} = A_{\text{EOB}}(\lambda_i, \theta_k)$ ,  $\phi_{\text{CE}}^{i,k} = \phi_{\text{EOB}}(\lambda_i, \theta_k)$ . At this

point we only retain the deviations at a log-spaced set of  $J = 10$  frequency nodes, defining

$$\delta A_j = \delta A(f_j) \quad (29)$$

$$\delta\phi_j = \delta\phi(f_j), \quad (30)$$

where the nodes  $\{f_j\}_{j=1}^J$  are spaced uniformly in logarithmic frequency in the interval  $\approx [20, 406]$  Hz, where the upper cutoff is determined from a maximum geometric frequency  $Mf_{\text{max}} = 0.1$  at a total mass of  $50M_{\odot}$ . We chose to use log-frequency spacing based on the note [56] on calibration uncertainty. This choice, along with the choice of ten nodes, seemed to capture the waveform uncertainty morphology reasonably well, particularly the increased structure at lower frequencies. For ease of notation, we drop the discrete frequency index in the following discussion.

Collecting the discrete deviations in a vector, we approximate these distributions with a multivariate normal ansatz

$$p\left((\vec{\delta A}, \vec{\delta\phi})|\lambda_i\right) \approx \mathcal{N}_{2J}(\vec{\mu}(\lambda_i), \Sigma(\lambda_i)), \quad (31)$$

with mean vectors  $\vec{\mu}(\lambda_i) \in \mathbb{R}^{2J}$  and covariance matrices  $\Sigma(\lambda_i) \in \mathbb{R}^{2J \times 2J}$ .

Finally, we use GPR [65] to interpolate this information over the parameter space, generalizing to arbitrary  $\lambda$  near the calibration points

$$(\vec{\mu}(\lambda_i), \Sigma(\lambda_i)) \mapsto (\vec{\mu}(\lambda), \Sigma(\lambda)). \quad (32)$$

To do this, it is advantageous to perform a Cholesky decomposition of each covariance matrix in order to preserve its positive semi-definiteness

$$\Sigma(\lambda_i) = L(\lambda_i)^T L(\lambda_i), \quad (33)$$

and we perform GPR interpolation on the set of  $\{\vec{\mu}(\lambda_i), L(\lambda_i)\}$ , where the lower triangular matrices  $L$  are suitably arranged into a vector. We only use the GPR means in the uncertainty model. In this implementation the stochasticity of the model comes entirely from the modeling of the covariances  $\Sigma(\lambda)$ .

### 2. Evaluation of calibration error model

The CE model allows for rapid draws of amplitude and phase deviation samples at a fixed parameter space point  $\lambda$

$$\left(\{\vec{\delta A}\}, \{\vec{\delta\phi}\}\right) \sim p((\delta A, \delta\phi)|\lambda). \quad (34)$$

These samples can be plugged into the CE model ansatz Eq. (25) to obtain a distribution of CE waveforms  $p(h_{\text{CE}}|\lambda)$ .

The GPR evaluation is achieved by (i) drawing multivariate normal vectors

$$\vec{\epsilon}_A, \vec{\epsilon}_\phi \sim \mathcal{N}_J(0, I), \quad (35)$$

(ii) evaluating the GPR fits for amplitude and phase mean vectors  $\vec{\mu}$  and the decomposed covariance matrices  $L$  at point  $\lambda$ , (iii) computing the amplitude and phase deviations

$$\vec{\delta A} = \vec{\mu}_A(\lambda) + L_A(\lambda)\vec{\epsilon}_A \quad (36)$$

$$\vec{\delta\phi} = \vec{\mu}_\phi(\lambda) + L_\phi(\lambda)\vec{\epsilon}_\phi, \quad (37)$$

(iv) constructing cubic splines for  $\delta A(f)$  and  $\delta\phi(f)$ , and evaluating the CE waveform Eq. (25) on the desired frequency grid. We refer to the uncertainty model as **SEOBNRv4CE** and, the mean uncertainty model with  $\vec{\epsilon} = 0$ , as **SEOBNRv4CE0**.

Fig. 2 shows the approximation of amplitude and phase differences by the uncertainty model for a simulation in the test set. They generally follow the same shape in frequency. As shown in Fig. 3, while the means are somewhat offset, the bulk of the uncertainty regions overlap. A linear difference in the phase may also be compensated by time and phase shifts. Indeed, the second panel of this figure shows that while the predicted match distribution extends to lower match values, it overlaps well with the actual match distribution.

Fig. 4 indicates that both for training and test configurations in some cases the uncertainty model does better than the calibration posteriors, and in other cases it is the opposite. The spread of the difference is somewhat larger for the test cases which is to be expected because the uncertainty model only approximates and interpolates the calibration posterior information. A similar picture is seen when comparing the full match distributions.

### 3. Interpretation of calibration error model

Parametrized by  $\vec{\epsilon}_A, \vec{\epsilon}_\phi$ , the **SEOBNRv4CE** model returns a distribution of waveforms with amplitude and phase deviations around the means  $\vec{\mu}_A(\lambda), \vec{\mu}_\phi(\lambda)$  which arise from interpolation of the mean deviations in amplitude and phase between the calibrated **SEOBNRv4** and the uncalibrated model conditioned on NR-calibration information.

For computational efficiency we use the frequency domain reduced-order-model (ROM) of **SEOBNRv4** [24, 67, 68] which closely approximates the time domain **SEOBNRv4** model:

$$\tilde{h}_{\text{CE}}(\lambda, \vec{\epsilon}; f) = \tilde{h}_{\text{ROM}}(\lambda; f) [1 + \delta A(\lambda, \vec{\epsilon}; f)] \exp(i\delta\phi(\lambda, \vec{\epsilon}; f)). \quad (38)$$

For the sake of comparison we also consider a deterministic waveform model where we assume a neutral or mean calibration  $\vec{\epsilon} = 0$  which we refer to as **SEOBNRv4CE0**. Because of the normal approximation and GPR interpolation of waveform differences used in **SEOBNRv4CE**,  $\vec{\epsilon} = 0$  does not exactly correspond to  $\delta A, \delta\phi = 0$  over the parameter space. Therefore **SEOBNRv4CE0** is close, but not exactly the same as the calibrated **SEOBNRv4** (or its ROM

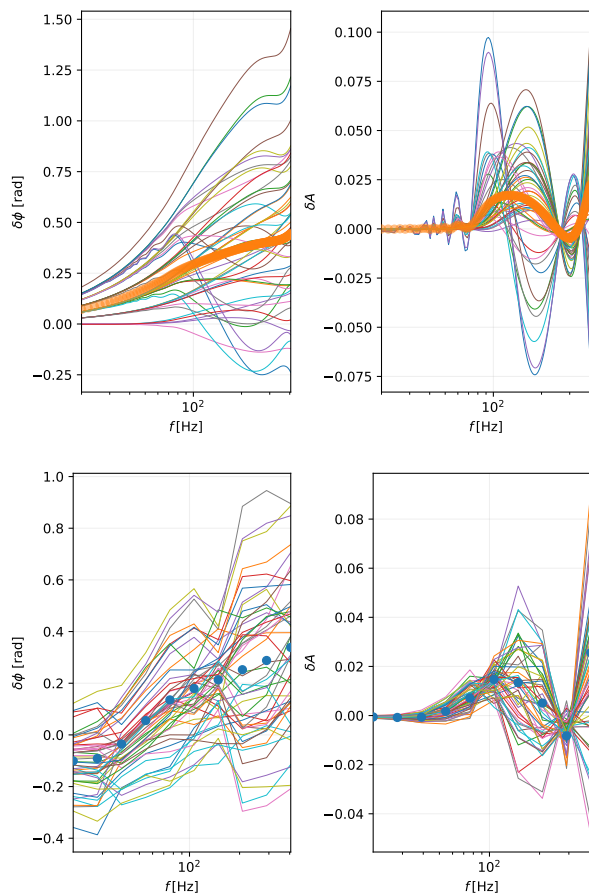


Figure 2. Actual (top) and predicted (bottom) amplitude and phase differences for **SXS\_BBH\_0166**  $q = 6.0, \chi_1 = 0.0, \chi_2 = 0.0$ . Actual differences are samples from the distribution defined in Eq.(28) while the differences predicted by the uncertainty model are given by Eq.(36). The mean differences are indicated by filled orange and blue circles in the top and bottom panels, respectively.

approximation). Indeed, Fig. 5 shows that the mean uncertainty model (**SEOBNRv4CE0**) is very close to **SEOBNRv4** and deviations reach about  $\sim 2\%$  in mismatch at the 95th percentile of the match distribution.

## F. Parameter estimation

The main goal of parameter estimation is to find the posterior distribution  $p(\Lambda|\{d_k\}, \mathcal{H})$  of the BBH parameters  $\Lambda$  using Bayes' theorem,

$$p(\Lambda|\{d_k\}, \mathcal{H}) = \frac{\mathcal{L}(\{d_k\}|\Lambda, \mathcal{H})\pi(\Lambda|\mathcal{H})}{\mathcal{Z}(\{d_k\}|\mathcal{H})}, \quad (39)$$

where  $\mathcal{H}$  is the signal hypothesis and  $d_i(t)$  is the time domain strain data in interferometer  $i$  of the LVK network.

The signal and template waveforms are projected on the interferometric GW detectors and we compute the

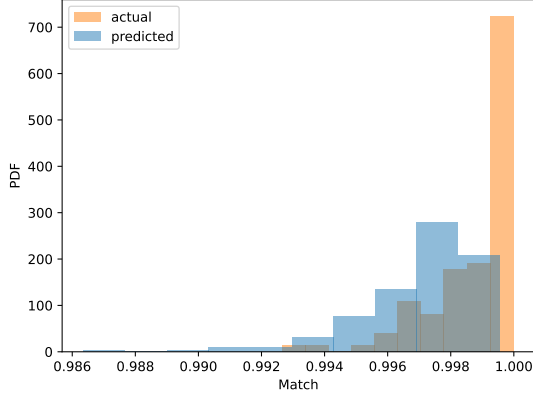
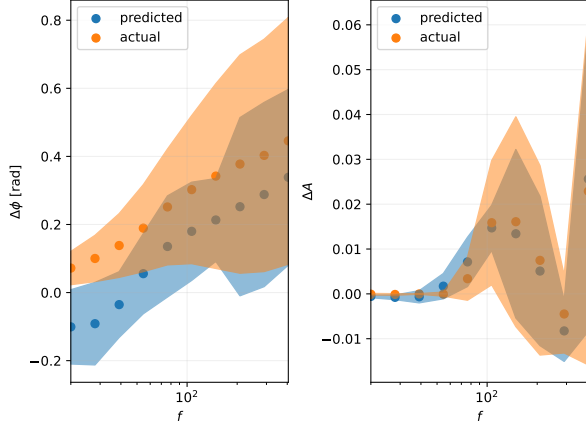


Figure 3. Top: comparison of actual and predicted means and  $1 - \sigma$  uncertainty (neglecting correlations between nodes at different frequencies) for the same configuration shown in Fig. 2. Bottom: matches between uncalibrated SEOBNRv4 at draws from calibration posterior and SEOBNRv4 (actual) and between the uncertainty model and SEOBNRv4 (predicted).

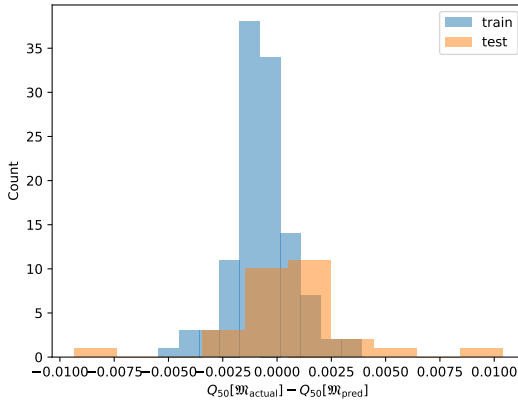


Figure 4. Difference between medians of matches between uncalibrated SEOBNRv4 at draws from calibration posterior and SEOBNRv4 ( $\mathfrak{M}_{\text{actual}}$ ) and matches between the uncertainty model and SEOBNRv4 ( $\mathfrak{M}_{\text{pred}}$ ) for both the training and test NR configurations.

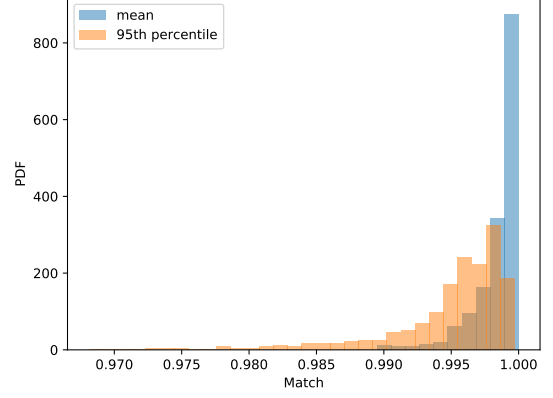


Figure 5. Histogram of matches between SEOBNRv4 and the SEOBNRv4CE uncertainty model, either assuming mean deviations ( $\bar{\epsilon} = 0$ , SEOBNRv4CE0) or the 95th percentile of the match distribution assuming Eq. (35).

strains from the GW polarizations and detector pattern functions [6]

$$h(t; \Lambda) = F_+(\text{ra, dec, } \psi)h_+(t; \Theta) + F_\times(\text{ra, dec, } \psi)h_\times(t; \Lambda) \quad (40)$$

The prior probability distribution  $\pi(\Lambda|\mathcal{H})$  in Eq. (39) encapsulates our prior knowledge of the distribution of  $\Lambda$  and  $\mathcal{L}(\{d_k\}|\Lambda, \mathcal{H})$  is the likelihood of observing the data  $d$  given an assumed waveform model  $h^{\mathcal{H}}(t; \Lambda)$ . The Whittle likelihood for stationary Gaussian noise for a network of detectors is [6, 9]

$$\mathcal{L}(\{d_i\}|\Lambda, \mathcal{H}) \propto \prod_i \exp\left(-\frac{1}{2}\langle d_i - h_i^{\mathcal{H}}(\Lambda) | d_i - h_i^{\mathcal{H}}(\Lambda) \rangle\right), \quad (41)$$

where  $\langle \cdot | \cdot \rangle$  is the noise-weighted inner product of Eq. (3).

The normalizing constant

$$\mathcal{Z}(\{d_i\}|\mathcal{H}) = \int d\Lambda \pi(\Lambda|\mathcal{H}) \mathcal{L}(\{d_i\}|\Lambda, \mathcal{H}) \quad (42)$$

in Eq. 39 is called evidence and can be used for model selection. The marginal posterior probability distribution on a subset of binary parameters  $\vec{\lambda}_A$ , where  $\Lambda = \{\vec{\lambda}_A, \vec{\lambda}_B\}$ , is defined as,

$$p(\vec{\lambda}_A|\{d_i\}, \mathcal{H}) = \int_{\vec{\lambda}_B} d\vec{\lambda}_B p(\vec{\lambda}_A|\{d_i\}, \mathcal{H}). \quad (43)$$

In this study we use the parameter estimation code Bilby [7, 8] and the nested sampling algorithm Dynesty [69, 70]. We choose an HLV network at advanced LIGO and advanced Virgo design sensitivity [71, 72]. We use an average *zero noise* realization in this study to focus on waveform systematics and avoid the effect of random Gaussian noise realizations on posteriors. With this assumption biases observed in posterior distributions can

arise from discrepancies in signal and template waveform models or prior effects.

We choose a uniform prior on chirp mass  $\mathcal{M} \sim \mathcal{U}[25, 50]M_\odot$  and mass-ratio  $1/q \sim \mathcal{U}[0.125, 1]$ , uniform priors for the dimensionless aligned spins of the component BHs  $\chi_i \sim \mathcal{U}[-0.8, 0.8]$  with limits arising from the calibration region of NRHybSur3dq8 [40]. We assume an isotropic prior for the location of the GW signal on the sky and a distance prior corresponding to a homogenous rate density in the nearby Universe. Finally, we choose  $\cos\theta_{\text{JN}} \sim \mathcal{U}[0, \pi]$  and a uniform prior in geocentric time  $t_c \sim \mathcal{U}[-0.1, 0.1]$  around the geocentric time of the injected signal.

When we perform inference with the SEOBNRv4CE uncertainty model we choose unit normal priors for the components of  $\epsilon$  following Eq. (35). We typically marginalize over these uncertainty parameters.

### III. PARAMETER ESTIMATION WITH WAVEFORM UNCERTAINTY

Here we test the effectiveness of the SEOBNRv4CE uncertainty model we introduced in Sec. II E by conducting a parameter estimation campaign using mock GW data. Our primary objective is to study systematic biases induced by the SEOBNRv4 waveform model and evaluate how well the SEOBNRv4CE model mitigates these effects.

#### A. Parameter estimation setup

In this study we use the waveform models SEOBNRv4\_ROM [24, 67, 68], and NRHybSur3dq8 [40], as available in the LALSuite [73] software package, in addition to the new uncertainty model SEOBNRv4CE we developed in Sec. II E.

SEOBNRv4\_ROM [24] is a frequency domain reduced order model (ROM) of the time domain SEOBNRv4 model [24] using the methodology developed in [67, 68]. It provides an accurate and computationally much faster representation of SEOBNRv4 waveforms. This model includes the  $(2, \pm 2)$  modes for non-precessing binary black holes and can be used for a wide range in mass-ratio and BH spin magnitudes up to maximal spin. The new uncertainty model we develop in this study is based on SEOBNRv4\_ROM and the set of calibration posteriors  $p(\theta|\lambda_i)$  obtained for SEOBNRv4. While SEOBNRv4 is not the newest SEOBNR model [74] the focus of this paper is more on showcasing an efficient method of marginalizing over waveform systematics in parameter estimation.

We use the NR-hybrid surrogate model NRHybSur3dq8 [40] as an independent and highly accurate comparison waveform for parameter estimation studies. NRHybSur3dq8 models BBHs with aligned spin magnitudes  $|\chi_i| \leq 0.8$  and mass-ratios smaller than  $q \leq 8$  and includes a set of higher harmonics up to  $\ell \sim 4$ . Here we only include the dominant  $(2, \pm 2)$  mode of

NRHybSur3dq8, so that all models can be compared on an equal footing.

We represent all signals by NRHybSur3dq8 to act as a stand-in for NR simulations because of its superior accuracy. We assume a zero noise realization and an HLV network at design sensitivity. Analyses follow the Bayesian framework laid out in Sec. II F to estimate the posterior distribution  $p(\Lambda|d, \mathcal{H})$  on BBH parameters. To explore how well the method works over parameter space we analyze a grid of signals defined as the Cartesian product of binary configurations: mass ratio  $q = \{1.25, 4, 8\}$ , aligned spin magnitude  $\chi_1 = \chi_2 = \{-0.5, 0, 0.5\}$ , luminosity distance  $d_L = \{205, 410, 820, 1640\}$  Mpc. Each signal is analyzed for four template waveform models: NRHybSur3dq8, SEOBNRv4, SEOBNRv4CE, and SEOBNRv4CEO.

Remaining signal parameters are kept fixed for each configuration: chirp mass  $\mathcal{M} = 32.0499M_\odot$ , inclination angle  $\iota = 2.83701491$  rad, polarization angle  $\psi = 1.42892206$  rad, coalescence phase  $\phi_c = 1.3$  rad, coalescence time  $t_c = 1126259462.0$  sec, right ascension  $\text{ra} = -1.26157296$  rad, and declination  $\text{dec} = 1.94972503$  rad. The prior distributions are provided in Sec. II F, and unless otherwise noted, we marginalize over the  $\epsilon$  parameters.

#### B. Parameter estimation results

In this section we discuss the results of the Bayesian analysis following the setup laid out in Sec. III A. We focus on the effect of waveform systematics on key intrinsic parameters chirp mass  $\mathcal{M}$ , mass ratio  $q$ , and effective spin  $\chi_{\text{eff}}$ . To estimate the statistical error for a given parameter  $\lambda$ , we calculate the standard deviation  $\sigma_\lambda$  of the one-dimensional marginal posterior distribution. To quantify how far the recovered posterior deviates from the true (injected) value  $\lambda_{\text{tr}}$ , we calculate the bias as  $\Delta\lambda = |\lambda_{\text{med}} - \lambda_{\text{tr}}|$ , where  $\lambda_{\text{med}}$  is the median of the posterior distribution. Then, the normalized bias is obtained by taking the ratio  $\Delta\lambda/\sigma_\lambda$ .

##### 1. Evolution of chirp mass posterior with SNR

Fig. 6 shows the evolution of the marginal chirp mass posterior at various distances  $d_L$ . We observe that as  $d_L$  decreases the distributions get narrower. This behavior is expected, as the SNR is proportional to  $1/d_L$ . Increased SNR leads to a reduction in statistical error as higher SNR improves the precision in parameter estimation. Because the signal is chosen as NRHybSur3dq8, the posterior distribution obtained with this model peaks around the true chirp mass value. The posterior obtained using SEOBNRv4 is significantly biased at higher SNR. Meanwhile, the posteriors obtained with SEOBNRv4CE show less bias compared to SEOBNRv4 at the expense of being less precise. At lower SNR, the posteriors from SEOBNRv4CE have similar

widths to those from NRHybSur3dq8, but at higher SNR, the SEOBNRv4CE posteriors are considerably wider.

In Fig. 7, we further analyze statistical uncertainties represented by the standard deviation  $\sigma$  of the one dimensional marginal posterior distribution as a function of SNR. We observe that the standard deviation of the SEOBNRv4CE chirp mass posterior is larger than that of the NRHybSur3dq8 posterior. Moreover, the disparity between the chirp mass standard deviations increases as the SNR rises. We also observe that the SEOBNRv4 posterior has similar standard deviation as the NRHybSur3dq8 posterior. Assuming that the joint posterior can be approximated by a multivariate Gaussian distribution at high SNR, we expect the posterior distributions for models which do not include waveform uncertainty to follow an inverse power law with slope  $-1$ . By fitting the data to the relation  $\sigma \propto \rho^{-\alpha}$ , we obtain  $\alpha = -0.77$  for NRHybSur3dq8,  $\alpha = -0.80$  for SEOBNRv4, and  $\alpha = -0.58$  for SEOBNRv4CE0. While we do not recover the ideal scaling for NRHybSur3dq8 and SEOBNRv4, we do see that the exponent is less negative for SEOBNRv4CE0 than the other models, reflecting the broader SEOBNRv4CE0 posteriors – see Sec. III B 4 for an analysis in a more idealized setting. This observation is consistent with posterior broadening in the Moore & Gair formalism[54], where the marginalized likelihood distribution over waveform uncertainty in Eq. 22 is wider compared to the standard likelihood function in Eq. 17. Because SEOBNRv4CE0 is cast as a model of amplitude and phase deviations rather than overall waveform differences we cannot directly access the increase in variance  $\sigma^2(\lambda)$  arising from marginalization over waveform uncertainty.

## 2. Parameter correlations

From the corner plot shown in Fig. 8, we can make several key observations. First, in both the non-spinning and spinning cases at mass-ratio  $q = 4$ , the NRHybSur3dq8 model accurately estimates the posterior, as it is the model used for the signal. In the left panel, which shows the non-spinning system, the bias in the SEOBNRv4 model is small, especially for chirp mass and mass-ratio. However, in the right panel (spinning system with  $\chi_{\text{eff}} = 0.5$ ), significant bias is observed across all three parameters shown in the plots, with almost no overlap in chirp mass and  $\chi_{\text{eff}}$ . When using the SEOBNRv4CE model, we observe bias in all recovered parameters ( $\mathcal{M}$ ,  $q$ , and  $\chi_{\text{eff}}$ ) in the non-spinning case, yet much of the bias apparent for SEOBNRv4 in the spinning system is mitigated by SEOBNRv4CE. SEOBNRv4 is expected to be less accurate for spinning systems. Lastly, we notice strong correlations amongst the BBH parameters, which may pose challenges for the SEOBNRv4CE model in effectively exploring the full parameter space. These correlations could explain some limitations in parameter recovery using SEOBNRv4CE model. We also point out that SEOBNRv4CE0 and SEOBNRv4 lead to different biases. For the non-spinning configuration in the left panel of Fig. 8

SEOBNRv4CE and SEOBNRv4CE0 show similarly large bias, much worse than the bias found for SEOBNRv4. However, for the spinning configuration shown in the right panel SEOBNRv4CE mitigates bias found for SEOBNRv4CE0 and SEOBNRv4CE0 performs better than SEOBNRv4.

## 3. Normalized bias over parameter space

In Fig. 9a we show normalized bias in chirp mass for signals varying over a 3 by 3 grid of mass-ratios and spins for a luminosity distance of  $d_L = 410$  Mpc. As expected, the bias is minimal for recovery with the NRHybSur3dq8 model. The bias tends to increase for the SEOBNRv4 model, especially for spinning configurations  $\chi_1 = \chi_2 = \pm 0.5$ . Much of this bias is mitigated with the SEOBNRv4CE model. However, we observe an overall increase in bias for non-spinning systems with the uncertainty model, compared to the SEOBNRv4 model. This may be due to the SEOBNRv4 model being better calibrated against NR simulations near zero spins [24] and the SEOBNRv4CE being less well calibrated there, as is also indicated by increased bias seen for SEOBNRv4CE0 for non-spinning binaries. Here, SEOBNRv4CE0 tends to perform better than SEOBNRv4 for positive aligned spins  $\chi_1 = \chi_2 = +0.5$ .

Because of our choice of constant distance for all signals shown in Fig. 9a the SNR varies with mass ratio and spin. The network SNR corresponding to each configuration is shown in the Fig. 9b. The comparable mass binary with positive aligned spin has highest SNR  $\sim 130$ .

Similarly, we plot the normalized bias for a set of corresponding configurations with luminosity distance  $d_L = 820$  Mpc in Fig 10a, which constitutes a lower SNR version of the systems shown in Fig. 9a. As expected, at lower SNRs, configurations are more affected by statistical errors, leading to broader posteriors. Consequently, the overall bias in chirp mass  $\mathcal{M}$  is reduced across the parameter space.

## 4. Idealized scaling

Finally, we seek to test our uncertainty model in a more simplistic situation. We select a *GW150914*-like signal using the NRHybSur3dq8 model. Accordingly we choose mass ratio  $q = 1.228$ , and aligned spins  $\chi_1 = -0.32$ ,  $\chi_2 = -0.57$ , and luminosity distance  $d_L = 410$  Mpc [47, 75]. The remaining parameters are set as for the other configurations discussed in Sec. III A. For this analysis, we only sample in chirp mass  $\mathcal{M}$ , coalescence time  $t_c$ , and relative phase  $\phi_c$ . All other parameters are pinned to the true parameter value of the signal. Fig. 11 shows the chirp mass posteriors. We witness significant bias for SEOBNRv4 model with no support at the true value. SEOBNRv4CE mitigates some of the bias in the chirp mass. Here, SEOBNRv4CE0 performs very well showing only a small amount of bias. In Fig. 12 we show the standard deviation of the chirp mass  $\sigma_{\mathcal{M}}$  as a function of

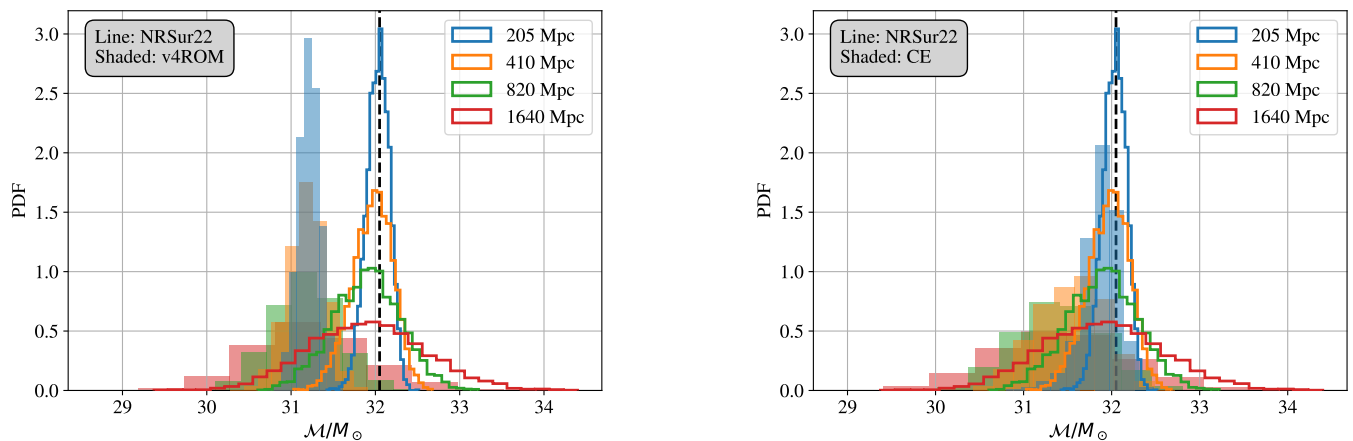


Figure 6. The evolution of the chirp mass posterior as a function of luminosity distance is presented for a binary configuration with mass ratio  $q = 4.0$  and spin magnitudes  $\chi_1 = \chi_2 = 0.5$ . The corresponding signal-to-noise ratios (SNRs) for luminosity distances  $d_L = 205$  Mpc, 410 Mpc, 820 Mpc, and 1640 Mpc are 217, 108, 54, and 27, respectively. The solid line illustrates the posterior recovered using NRHybSur3dq8. In the left plot, the shaded area represents the posterior obtained with SEOBv4, while the right plot shows the posterior distribution from SEOBv4CE. We observe significant bias in the SEOBv4 posterior at higher SNRs, whereas much of this bias is mitigated in the SEOBv4CE model. However, the SEOBv4CE posterior distribution is considerably broader.

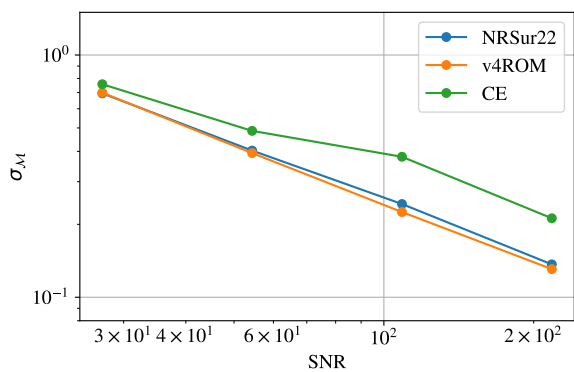


Figure 7. Standard deviation of chirp mass posterior as a function of SNR for the configuration  $q = 4$ ,  $\chi_1 = 0.5$ ,  $\chi_2 = 0.5$  also shown in Fig. 6 for waveform models NRHybSur3dq8, SEOBv4, and SEOBv4CE.

SNR. In this idealistic situation both NRHybSur3dq8 and SEOBv4 have a close to ideal power exponent  $\alpha \sim -1$ . For SEOBv4CE we obtain  $\alpha = -0.75$ , which again corresponds to wider posterior distributions compared to models which do not include waveform uncertainty for all values of SNR.

#### IV. CONCLUSION

In this paper, we develop a novel probabilistic waveform model, SEOBv4CE, as an alternative to the deterministic SEOBv4 model. As discussed in Sec. II E SEOBv4CE uses a multivariate normal approximation, Eq. (31), of

amplitude and phase deviations of GW data from the calibrated SEOBv4 model and the uncalibrated SEOBv4 model evaluated at draws from the calibration posterior samples  $p(\theta|\lambda_i)$ . We use Gaussian Process Regression (GPR) to interpolate the means and Cholesky decomposition of covariance matrices of these deviations. The resulting model  $\tilde{h}_{CE}(\lambda, \vec{\epsilon}, f)$  consisting of Eqs. (38), (36), and (35) can be efficiently computed in the Fourier domain. We predict the amplitude and phase deviations at ten frequency nodes and therefore SEOBv4CE depends on twenty parameters  $\vec{\epsilon}$  which capture NR calibration uncertainty in the SEOBv4 model.

Unlike Moore and Gair [54] who directly model waveform deviations  $\delta h$  we cannot analytically marginalize over waveform uncertainty because of our amplitude phase parametrization, even though we are also using GPR. We perform a Bayesian inference study where we marginalize over all uncertainty parameters. By doing so, we are able to incorporate waveform systematics arising from the calibration process in the SEOBv4 model.

We evaluate the effectiveness of the SEOBv4CE model by performing a detailed PE study using mock GW signals described in Sec. III. We analyze NRHybSur3dq8 signals in zero noise for variety of BBH configurations over the binary parameter space and recover the posterior using four template models – NRHybSur3dq8, SEOBv4, SEOBv4CE, and SEOBv4CE0. We find that a PE analysis using SEOBv4CE takes only a factor of two longer than an analysis with SEOBv4, even though the uncertainty model needs to (i) evaluate the GPR of amplitude and phase deviations, compute a complex exponential, and multiply the corrections with the base model, and (ii) sample in twenty additional uncertainty parameters. Our results demonstrate that, for most cases, the uncertainty

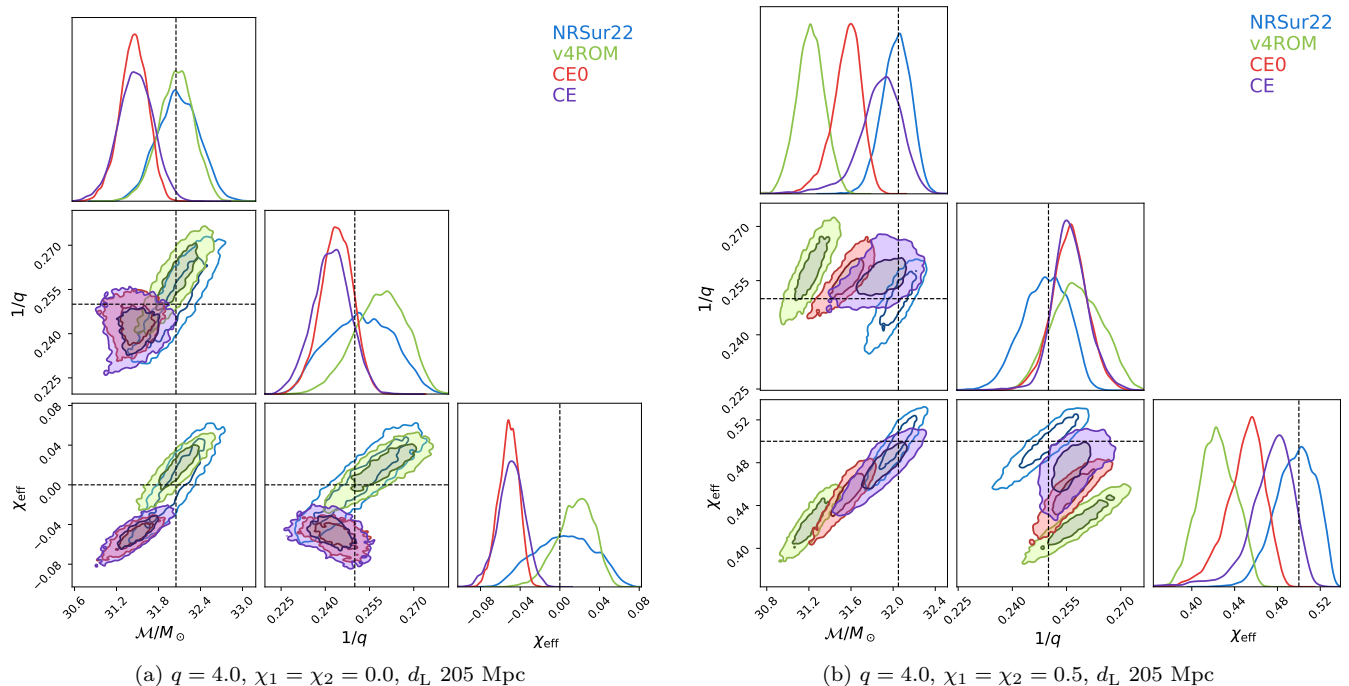


Figure 8. Partial corner plots illustrating the posterior distributions for chirp mass  $\mathcal{M}$ , mass ratio  $q$ , and effective spin  $\chi_{\text{eff}}$ , derived from Bayesian PE using four different waveform models: NRHybSur3dq8, SEOBNRv4, SEOBNRv4CE, and SEOBNRv4CE0. The left panel shows results for a non-spinning system, while the right panel displays results for a spinning system with  $\chi_1 = \chi_2 = 0.5$  and mass ratio  $q = 4$ . The diagonal panels present the marginalized one-dimensional posterior distributions for each parameter, while the off-diagonal panels depict the two-dimensional joint posterior distributions between pairs of parameters. The contours in the two-dimensional plots represent the 50% and 90% credible regions. The true injected values of the parameters are indicated by the dashed black lines.

model reduces bias compared to the standard SEOBNRv4 model in parameter recovery. Such bias is expected for high SNR signals and when waveform systematics dominate over statistical uncertainties. In particular, we observe a broadening of SEOBNRv4CE posteriors compared to those of other models (see Figs. 7 and 12), together with a reduction in bias for most configurations (see Figs 6, 8, and 11).

Our investigation of normalized biases over parameter space (see Fig. 9a) reveals that systematic biases for SEOBNRv4 arise predominantly for spinning configurations, for which SEOBNRv4 is less well calibrated against NR than for non-spinning configurations. This is especially true for unequal mass configurations with moderately high positive aligned spin, but we also encountered biases for a near equal mass configuration with negative aligned spins. Some of this effect may be due to the lower density of NR simulations available for calibration, and some due to the challenge of accurately modeling the more complicated physics of spinning binaries.

The uncertainty model proved to be effective in mitigating biases for spinning configurations – reducing normalized biases by a factor of  $\sim 1.5$  or more; however, for non-spinning binaries, where SEOBNRv4 is already well calibrated, PE with SEOBNRv4CE model fell short of mitigating biases. This limitation may stem from the sim-

plifying assumption that the metric entering the GPR covariance function, Eq. (10) in Sec. II B is diagonal, containing learnable length scale hyper-parameters for mass ratio and aligned spins. Realistically, one should take into account correlations between intrinsic BBH parameters in the choice of GPR hyper-parameters. We may explore this possibility in a future work.

We demonstrated that chirp mass posteriors for SEOBNRv4CE are wider in terms of the standard deviation than those of models which do not include waveform uncertainty. In an idealized setting where most waveform parameters are pinned and we only sample in chirp mass, time and phase, we found that the standard deviations for SEOBNRv4 or NRHybSur3dq8 decrease inversely with SNR, in agreement with the behavior of a Gaussian posterior, whereas the standard deviation for SEOBNRv4CE decreases more slowly, at a power-law rate of  $-0.75$ , compared to the ideal exponent of  $-1$ , as also predicted by Moore and Gair [54] (see the increased variance in Eq. (22)).

Moore and Gair [54] proposed a likelihood function which marginalizes analytically over waveform uncertainty using a Gaussian process prior on the waveform difference  $\delta h$ . Their analysis was restricted to sampling the chirp mass and they assumed the model errors to be frequency independent. Our uncertainty model takes into account correlations in frequency for amplitude and phase

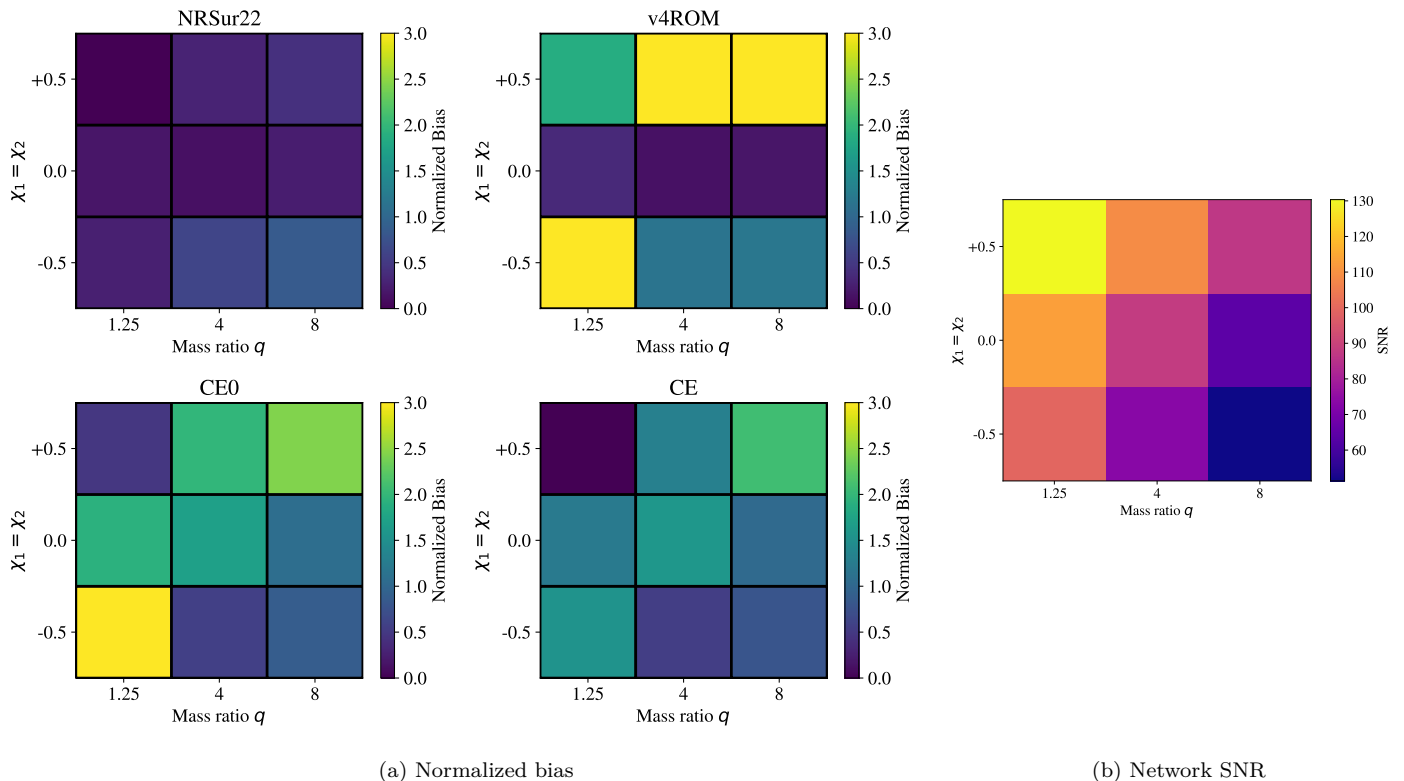


Figure 9. Left figure: Normalized biases for chirp mass over a grid of NRHybSure3q8 signals with varying mass ratio  $q$  and aligned spins  $\chi_1 = \chi_2$  at a luminosity distance of 410 Mpc. The signals are recovered with four waveform models *top left*: NRHybSure3q8, *top right*: SEOBNRv4, *bottom left*: SEOBNRv4CEO, and *bottom right*: SEOBNRv4CE. Right figure shows the network SNR of the injected signals for the given luminosity distance.

at a set of frequency nodes. Edelman *et al.* [58] instead explored the implications of unmodeled physics in GW observations. They augment an existing waveform model with unknown amplitude and phase deviations in the Fourier domain and infer posterior distributions for these deviations to constrain potential deviations from known physics accurately, instead of marginalizing over them. Read [59] introduces a frequency-dependent characterization of waveform error in amplitude and phase for binary neutron star signals and demonstrates how these differences can be marginalized over during the inference using technique similar to those applied in detector calibration. Lastly, Owen *et al.* [60] use Bayesian inference to assess the inaccuracies in theoretical waveform models due to missing higher-order PN terms. By treating these missing terms as unknown parameters and marginalizing over them with uninformed priors, the authors show improved parameter estimates, at the cost of higher statistical error.

While techniques for modeling and incorporating waveform uncertainty into PE have been explored in a few studies, they are not yet used as part of routine analyses carried out by the LVK collaboration. Clearly, more work needs to be done on the waveform side to construct waveform uncertainty models for more complete waveform models, including important physical effects such as precession, and eccentricity, and including higher or-

der modes. However, such techniques also need to be efficient and reliable before they will find adoption in large scale data analysis. Given that progress in directly improving the accuracy of waveform models to the levels required of third generation detectors will be very challenging, constrained by practical modeling assumptions and, most importantly, the availability of a dense set of high accuracy NR simulations covering binary parameter space, marginalization over waveform uncertainty should be a promising path to follow to enhance the fidelity of parameter estimates.

## ACKNOWLEDGMENTS

We wish to thank Christopher Moore, Vivien Raymond, Roberto Cotesta, Sergei Ossokine, and Alessandra Buonanno for contributions during the early part of this project. We would like to thank Jonathan Gair and Lorenzo Pompili, and Carl Haster for helpful discussions. The authors acknowledge support from the URI Center for Computational Research. In particular, the computations were performed on the UMass-URI UNITY high-performance computing cluster as well as the Hypatia computer cluster at the Max Planck Institute for Gravitational Physics in Potsdam-Golm, Germany. This material

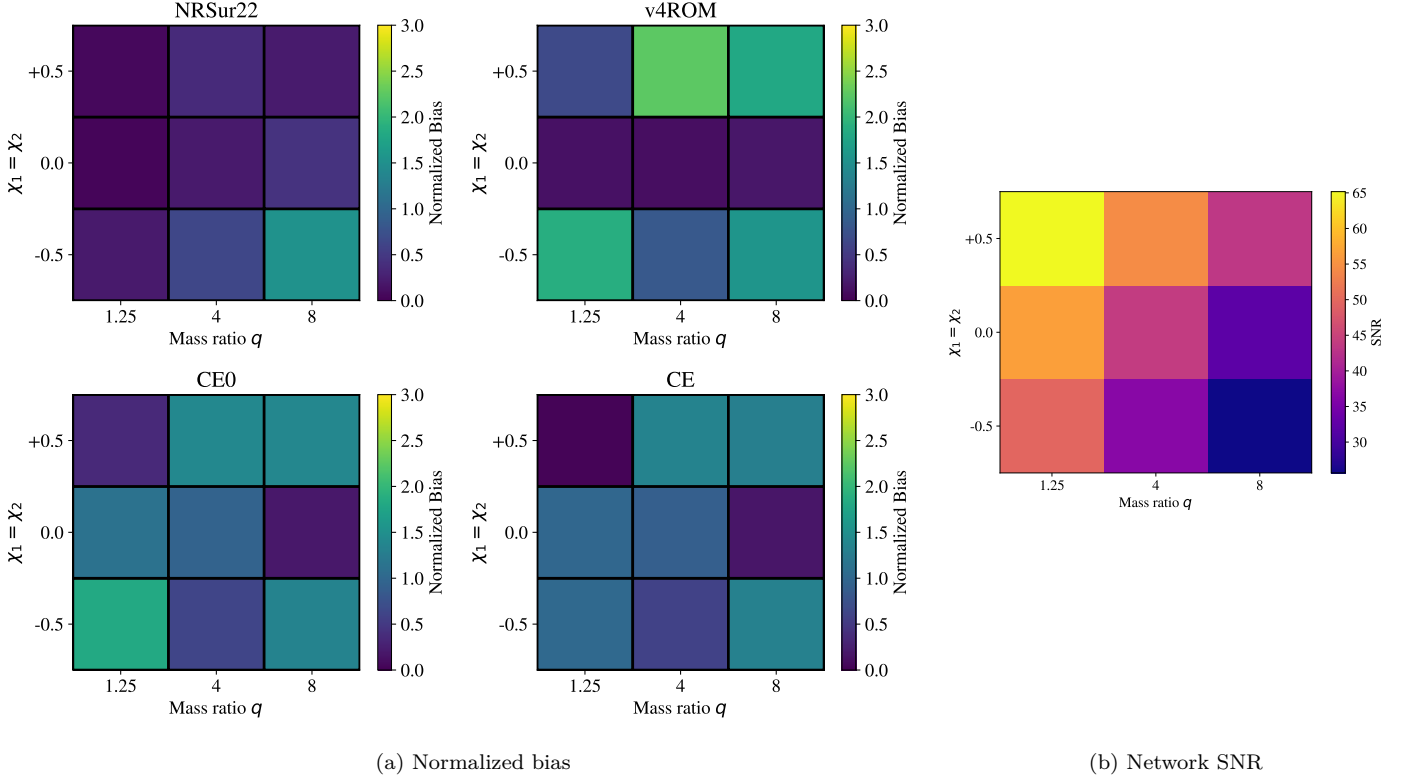


Figure 10. Normalized biases for chirp mass as shown in Fig. 9a except for a farther distance  $d_L = 820$  Mpc, which corresponds to lower SNRs. For ease of comparison with Fig. 9a we have kept the same limits on the normalized bias scale and colormap. Corresponding network SNR is given in the right figure.

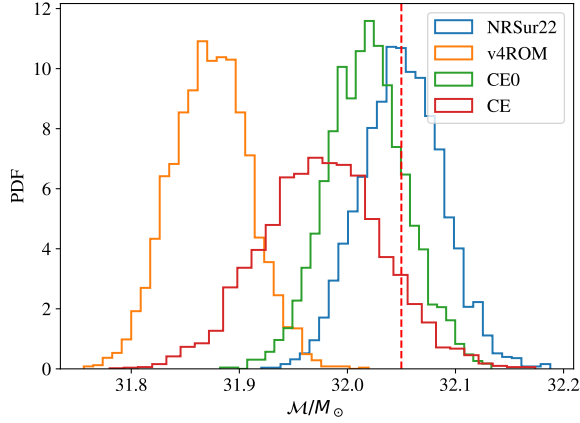


Figure 11. Chirp mass posterior of GW150914-like NRHybSur3dq8 signal recovered with waveform models NRHybSur3dq8, SEOBNrv4, SEOBNrv4CE0, and SEOBNrv4CE. The network SNR corresponding to this event is 111.5.

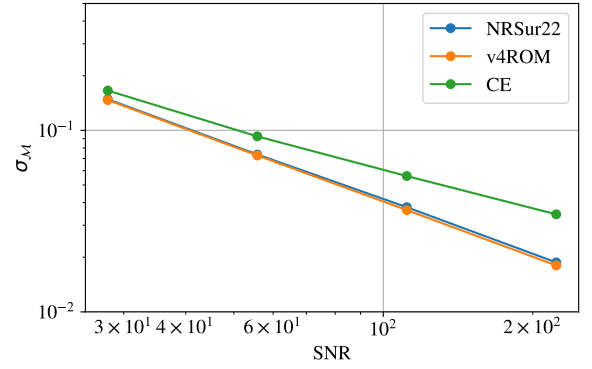


Figure 12. Standard deviation of chirp mass posterior as a function of SNR for the GW150914-like signal shown in Fig. 11. We find slopes  $\alpha = -0.99$  for NRHybSur3dq8,  $\alpha = -1.00$  for SEOBNrv4, and  $\alpha = -0.75$  for SEOBNrv4CE.

is based upon work supported by NSF's LIGO Laboratory which is a major facility fully funded by the NSF.

## REFERENCES

- [1] J. Aasi *et al.* (LIGO Scientific), Advanced LIGO, *Class. Quant. Grav.* **32**, 074001 (2015), arXiv:1411.4547 [gr-qc].
- [2] F. Acernese *et al.* (VIRGO), Advanced Virgo: a second-generation interferometric gravitational wave detector, *Class. Quant. Grav.* **32**, 024001 (2015), arXiv:1408.3978 [gr-qc].
- [3] T. Akutsu *et al.* (KAGRA), Overview of KAGRA: Detector design and construction history, *PTEP* **2021**, 05A101 (2021), arXiv:2005.05574 [physics.ins-det].
- [4] R. Abbott *et al.* (KAGRA, VIRGO, LIGO Scientific), GWTC-3: Compact Binary Coalescences Observed by LIGO and Virgo during the Second Part of the Third Observing Run, *Phys. Rev. X* **13**, 041039 (2023), arXiv:2111.03606 [gr-qc].
- [5] R. Abbott *et al.* (LIGO Scientific, VIRGO), GWTC-2.1: Deep extended catalog of compact binary coalescences observed by LIGO and Virgo during the first half of the third observing run, *Phys. Rev. D* **109**, 022001 (2024), arXiv:2108.01045 [gr-qc].
- [6] K. Chatziioannou, T. Dent, M. Fishbach, F. Ohme, M. Pürrer, V. Raymond, and J. Veitch, Compact binary coalescences: gravitational-wave astronomy with ground-based detectors, (2024), arXiv:2409.02037 [gr-qc].
- [7] G. Ashton *et al.*, BILBY: A user-friendly Bayesian inference library for gravitational-wave astronomy, *Astrophys. J. Suppl.* **241**, 27 (2019), arXiv:1811.02042 [astro-ph.IM].
- [8] I. M. Romero-Shaw *et al.*, Bayesian inference for compact binary coalescences with bilby: validation and application to the first LIGO–Virgo gravitational-wave transient catalogue, *Mon. Not. Roy. Astron. Soc.* **499**, 3295 (2020), arXiv:2006.00714 [astro-ph.IM].
- [9] E. Thrane and C. Talbot, An introduction to Bayesian inference in gravitational-wave astronomy: parameter estimation, model selection, and hierarchical models, *Publ. Astron. Soc. Austral.* **36**, e010 (2019), [Erratum: *Publ. Astron. Soc. Austral.* 37, e036 (2020)], arXiv:1809.02293 [astro-ph.IM].
- [10] J. Veitch *et al.*, Robust parameter estimation for compact binaries with ground-based gravitational-wave observations using the LALInference software library, *Phys. Rev. D* **91**, 042003 (2015), arXiv:1409.7215 [gr-qc].
- [11] S. Khan, S. Husa, M. Hannam, F. Ohme, M. Pürrer, X. Jiménez Forteza, and A. Bohé, Frequency-domain gravitational waves from nonprecessing black-hole binaries. II. A phenomenological model for the advanced detector era, *Phys. Rev.* **D93**, 044007 (2016), arXiv:1508.07253 [gr-qc].
- [12] G. Pratten, S. Husa, C. Garcia-Quiros, M. Colleoni, A. Ramos-Buades, H. Estelles, and R. Jaume, Setting the cornerstone for a family of models for gravitational waves from compact binaries: The dominant harmonic for nonprecessing quasicircular black holes, *Phys. Rev. D* **102**, 064001 (2020), arXiv:2001.11412 [gr-qc].
- [13] L. London, S. Khan, E. Fauchon-Jones, C. García, M. Hannam, S. Husa, X. Jiménez-Forteza, C. Kalaghatgi, F. Ohme, and F. Pannarale, First higher-multipole model of gravitational waves from spinning and coalescing black-hole binaries, *Phys. Rev. Lett.* **120**, 161102 (2018), arXiv:1708.00404 [gr-qc].
- [14] C. García-Quirós, M. Colleoni, S. Husa, H. Estellés, G. Pratten, A. Ramos-Buades, M. Mateu-Lucena, and R. Jaume, Multimode frequency-domain model for the gravitational wave signal from nonprecessing black-hole binaries, *Phys. Rev. D* **102**, 064002 (2020), arXiv:2001.10914 [gr-qc].
- [15] M. Hannam, P. Schmidt, A. Bohé, L. Haegel, S. Husa, F. Ohme, G. Pratten, and M. Pürrer, Simple Model of Complete Precessing Black-Hole-Binary Gravitational Waveforms, *Phys. Rev. Lett.* **113**, 151101 (2014), arXiv:1308.3271 [gr-qc].
- [16] G. Pratten *et al.*, Computationally efficient models for the dominant and subdominant harmonic modes of precessing binary black holes, *Phys. Rev. D* **103**, 104056 (2021), arXiv:2004.06503 [gr-qc].
- [17] E. Hamilton, L. London, J. E. Thompson, E. Fauchon-Jones, M. Hannam, C. Kalaghatgi, S. Khan, F. Pannarale, and A. Vano-Vinuales, Model of gravitational waves from precessing black-hole binaries through merger and ring-down, *Phys. Rev. D* **104**, 124027 (2021), arXiv:2107.08876 [gr-qc].
- [18] H. Estellés, A. Ramos-Buades, S. Husa, C. García-Quirós, M. Colleoni, L. Haegel, and R. Jaume, Phenomenological time domain model for dominant quadrupole gravitational wave signal of coalescing binary black holes, *Phys. Rev. D* **103**, 124060 (2021), arXiv:2004.08302 [gr-qc].
- [19] H. Estellés, S. Husa, M. Colleoni, D. Keitel, M. Mateu-Lucena, C. García-Quirós, A. Ramos-Buades, and A. Borchers, Time-domain phenomenological model of gravitational-wave subdominant harmonics for quasicircular nonprecessing binary black hole coalescences, *Phys. Rev. D* **105**, 084039 (2022), arXiv:2012.11923 [gr-qc].
- [20] H. Estellés, M. Colleoni, C. García-Quirós, S. Husa, D. Keitel, M. Mateu-Lucena, M. d. L. Planas, and A. Ramos-Buades, New twists in compact binary waveform modeling: A fast time-domain model for precession, *Phys. Rev. D* **105**, 084040 (2022), arXiv:2105.05872 [gr-qc].
- [21] T. Dietrich, S. Bernuzzi, and W. Tichy, Closed-form tidal approximants for binary neutron star gravitational waveforms constructed from high-resolution numerical relativity simulations, *Phys. Rev. D* **96**, 121501 (2017), arXiv:1706.02969 [gr-qc].
- [22] T. Dietrich, A. Samajdar, S. Khan, N. K. Johnson-McDaniel, R. Dudi, and W. Tichy, Improving the NRTidal model for binary neutron star systems, *Phys. Rev. D* **100**, 044003 (2019), arXiv:1905.06011 [gr-qc].
- [23] J. E. Thompson, E. Fauchon-Jones, S. Khan, E. Nitoglia, F. Pannarale, T. Dietrich, and M. Hannam, Modeling the gravitational wave signature of neutron star black hole coalescences, *Phys. Rev. D* **101**, 124059 (2020), arXiv:2002.08383 [gr-qc].
- [24] A. Bohé *et al.*, Improved effective-one-body model of spinning, nonprecessing binary black holes for the era of gravitational-wave astrophysics with advanced detectors, *Phys. Rev.* **D95**, 044028 (2017), arXiv:1611.03703 [gr-qc].
- [25] R. Cotesta, A. Buonanno, A. Bohé, A. Taracchini, I. Hinder, and S. Ossokine, Enriching the Symphony of Gravitational Waves from Binary Black Holes by Tuning Higher Harmonics, *Phys. Rev.* **D98**, 084028 (2018), arXiv:1803.10701 [gr-qc].
- [26] L. Pompili *et al.*, Laying the foundation of the effective-one-body waveform models SEOBNRv5: Improved accuracy and efficiency for spinning nonprecessing binary black

- holes, *Phys. Rev. D* **108**, 124035 (2023), arXiv:2303.18039 [gr-qc].
- [27] S. Ossokine *et al.*, Multipolar Effective-One-Body Waveforms for Precessing Binary Black Holes: Construction and Validation, *Phys. Rev. D* **102**, 044055 (2020), arXiv:2004.09442 [gr-qc].
- [28] A. Ramos-Buades, A. Buonanno, H. Estellés, M. Khalil, D. P. Mihaylov, S. Ossokine, L. Pompili, and M. Shiferaw, Next generation of accurate and efficient multipolar precessing-spin effective-one-body waveforms for binary black holes, *Phys. Rev. D* **108**, 124037 (2023), arXiv:2303.18046 [gr-qc].
- [29] J. Steinhoff, T. Hinderer, A. Buonanno, and A. Taracchini, Dynamical Tides in General Relativity: Effective Action and Effective-One-Body Hamiltonian, *Phys. Rev. D* **94**, 104028 (2016), arXiv:1608.01907 [gr-qc].
- [30] A. Matas *et al.*, Aligned-spin neutron-star-black-hole waveform model based on the effective-one-body approach and numerical-relativity simulations, *Phys. Rev. D* **102**, 043023 (2020), arXiv:2004.10001 [gr-qc].
- [31] A. Nagar *et al.*, Time-domain effective-one-body gravitational waveforms for coalescing compact binaries with nonprecessing spins, tides and self-spin effects, *Phys. Rev. D* **98**, 104052 (2018), arXiv:1806.01772 [gr-qc].
- [32] A. Nagar, F. Messina, P. Rettengo, D. Bini, T. Damour, A. Gericco, S. Akçay, and S. Bernuzzi, Nonlinear-in-spin effects in effective-one-body waveform models of spin-aligned, inspiralling, neutron star binaries, *Phys. Rev. D* **99**, 044007 (2019), arXiv:1812.07923 [gr-qc].
- [33] S. Akçay, S. Bernuzzi, F. Messina, A. Nagar, N. Ortiz, and P. Rettengo, Effective-one-body multipolar waveform for tidally interacting binary neutron stars up to merger, *Phys. Rev. D* **99**, 044051 (2019), arXiv:1812.02744 [gr-qc].
- [34] S. Akçay, R. Gamba, and S. Bernuzzi, Hybrid post-Newtonian effective-one-body scheme for spin-precessing compact-binary waveforms up to merger, *Phys. Rev. D* **103**, 024014 (2021), arXiv:2005.05338 [gr-qc].
- [35] R. Gamba, S. Akçay, S. Bernuzzi, and J. Williams, Effective-one-body waveforms for precessing coalescing compact binaries with post-Newtonian twist, *Phys. Rev. D* **106**, 024020 (2022), arXiv:2111.03675 [gr-qc].
- [36] S. E. Field, C. R. Galley, J. S. Hesthaven, J. Kaye, and M. Tiglio, Fast Prediction and Evaluation of Gravitational Waveforms Using Surrogate Models, **4**, 031006 (2014), arXiv:1308.3565 [gr-qc].
- [37] J. Blackman, S. E. Field, M. A. Scheel, C. R. Galley, D. A. Hemberger, P. Schmidt, and R. Smith, A Surrogate Model of Gravitational Waveforms from Numerical Relativity Simulations of Precessing Binary Black Hole Mergers, *Phys. Rev. D* **95**, 104023 (2017), arXiv:1701.00550 [gr-qc].
- [38] J. Blackman, S. E. Field, M. A. Scheel, C. R. Galley, C. D. Ott, M. Boyle, L. E. Kidder, H. P. Pfeiffer, and B. Szilágyi, Numerical relativity waveform surrogate model for generically precessing binary black hole mergers, *Phys. Rev. D* **96**, 024058 (2017), arXiv:1705.07089 [gr-qc].
- [39] V. Varma, S. E. Field, M. A. Scheel, J. Blackman, D. Gerosa, L. C. Stein, L. E. Kidder, and H. P. Pfeiffer, Surrogate models for precessing binary black hole simulations with unequal masses, *Phys. Rev. Research* **1**, 033015 (2019), arXiv:1905.09300 [gr-qc].
- [40] V. Varma, S. E. Field, M. A. Scheel, J. Blackman, L. E. Kidder, and H. P. Pfeiffer, Surrogate model of hybridized numerical relativity binary black hole waveforms, *Phys. Rev. D* **99**, 064045 (2019), arXiv:1812.07865 [gr-qc].
- [41] T. Islam, V. Varma, J. Lodman, S. E. Field, G. Khanna, M. A. Scheel, H. P. Pfeiffer, D. Gerosa, and L. E. Kidder, Eccentric binary black hole surrogate models for the gravitational waveform and remnant properties: comparable mass, nonspinning case, *Phys. Rev. D* **103**, 064022 (2021), arXiv:2101.11798 [gr-qc].
- [42] G. Ashton and S. Khan, Multiwaveform inference of gravitational waves, *Phys. Rev. D* **101**, 064037 (2020), arXiv:1910.09138 [gr-qc].
- [43] A. Z. Jan, A. B. Yelikar, J. Lange, and R. O’Shaughnessy, Assessing and marginalizing over compact binary coalescence waveform systematics with RIFT, *Phys. Rev. D* **102**, 124069 (2020), arXiv:2011.03571 [gr-qc].
- [44] G. Ashton and T. Dietrich, The use of hypermodels to understand binary neutron star collisions, *Nature Astron.* **6**, 961 (2022), arXiv:2111.09214 [gr-qc].
- [45] C. Hoy, Accelerating multimodel Bayesian inference, model selection, and systematic studies for gravitational wave astronomy, *Phys. Rev. D* **106**, 083003 (2022), arXiv:2208.00106 [gr-qc].
- [46] C. Hoy, S. Akçay, J. Mac Uilliam, and J. E. Thompson, Incorporating model accuracy into gravitational-wave Bayesian inference, (2024), arXiv:2409.19404 [gr-qc].
- [47] B. P. Abbott *et al.* (LIGO Scientific, Virgo), Effects of waveform model systematics on the interpretation of GW150914, *Class. Quant. Grav.* **34**, 104002 (2017), arXiv:1611.07531 [gr-qc].
- [48] M. Pürrer and C.-J. Haster, Gravitational waveform accuracy requirements for future ground-based detectors, *Phys. Rev. Res.* **2**, 023151 (2020), arXiv:1912.10055 [gr-qc].
- [49] A. Dhani, S. Völkel, A. Buonanno, H. Estelles, J. Gair, H. P. Pfeiffer, L. Pompili, and A. Toubiana, Systematic Biases in Estimating the Properties of Black Holes Due to Inaccurate Gravitational-Wave Models, (2024), arXiv:2404.05811 [gr-qc].
- [50] V. Kapil, L. Reali, R. Cotesta, and E. Berti, Systematic bias from waveform modeling for binary black hole populations in next-generation gravitational wave detectors, *Phys. Rev. D* **109**, 104043 (2024), arXiv:2404.00090 [gr-qc].
- [51] D. Ferguson, K. Jani, P. Laguna, and D. Shoemaker, Assessing the readiness of numerical relativity for LISA and 3G detectors, *Phys. Rev. D* **104**, 044037 (2021), arXiv:2006.04272 [gr-qc].
- [52] Q. Hu and J. Veitch, Assessing the model waveform accuracy of gravitational waves, *Phys. Rev. D* **106**, 044042 (2022), arXiv:2205.08448 [gr-qc].
- [53] A. Jan, D. Ferguson, J. Lange, D. Shoemaker, and A. Zimmerman, Accuracy limitations of existing numerical relativity waveforms on the data analysis of current and future ground-based detectors, *Phys. Rev. D* **110**, 024023 (2024), arXiv:2312.10241 [gr-qc].
- [54] C. J. Moore and J. R. Gair, Novel Method for Incorporating Model Uncertainties into Gravitational Wave Parameter Estimates, *Phys. Rev. Lett.* **113**, 251101 (2014), arXiv:1412.3657 [gr-qc].
- [55] C. J. Moore, C. P. L. Berry, A. J. K. Chua, and J. R. Gair, Improving gravitational-wave parameter estimation using Gaussian process regression, *Phys. Rev. D* **93**, 064001 (2016), arXiv:1509.04066 [gr-qc].
- [56] W. M. Farr, B. Farr, and T. Littenberg, *Modelling Calibration Errors In CBC Waveforms*, Tech. Rep. LIGO-T1400682 (LIGO Project, 2015).
- [57] S. Vitale, W. Del Pozzo, T. G. F. Li, C. Van Den Broeck,

- I. Mandel, B. Aylott, and J. Veitch, Effect of calibration errors on Bayesian parameter estimation for gravitational wave signals from inspiral binary systems in the Advanced Detectors era, *Phys. Rev. D* **85**, 064034 (2012), arXiv:1111.3044 [gr-qc].
- [58] B. Edelman *et al.*, Constraining unmodeled physics with compact binary mergers from GWTC-1, *Phys. Rev. D* **103**, 042004 (2021), arXiv:2008.06436 [gr-qc].
- [59] J. S. Read, Waveform uncertainty quantification and interpretation for gravitational-wave astronomy, *Class. Quant. Grav.* **40**, 135002 (2023), arXiv:2301.06630 [gr-qc].
- [60] C. B. Owen, C.-J. Haster, S. Perkins, N. J. Cornish, and N. Yunes, Waveform accuracy and systematic uncertainties in current gravitational wave observations, *Phys. Rev. D* **108**, 044018 (2023), arXiv:2301.11941 [gr-qc].
- [61] Z. Doctor, B. Farr, D. E. Holz, and M. Pürrer, Statistical Gravitational Waveform Models: What to Simulate Next?, *Phys. Rev. D* **96**, 123011 (2017), arXiv:1706.05408 [astro-ph.HE].
- [62] D. Williams, I. S. Heng, J. Gair, J. A. Clark, and B. Khamesra, Precessing numerical relativity waveform surrogate model for binary black holes: A Gaussian process regression approach, *Phys. Rev. D* **101**, 063011 (2020), arXiv:1903.09204 [gr-qc].
- [63] T. Andrade, R. Gamba, and J. Trenado, Actively learning numerical relativity, *Phys. Rev. D* **110**, 024080 (2024), arXiv:2311.11311 [gr-qc].
- [64] L. Pompili, A. Buonanno, and M. Pürrer, Accounting for Numerical-Relativity Calibration Uncertainty in Gravitational-Wave Modeling and Inference, in prep.
- [65] C. E. Rasmussen and C. K. I. Williams, *Gaussian Processes for Machine Learning*, by C.E. Rasmussen and C.K.I. Williams. ISBN-13 978-0-262-18253-9 (The MIT Press, 2006).
- [66] D. MacKay, *Information Theory, Inference, and Learning Algorithms* (Cambridge University Press, 2003).
- [67] M. Pürrer, Frequency domain reduced order models for gravitational waves from aligned-spin compact binaries, *Class. Quant. Grav.* **31**, 195010 (2014), arXiv:1402.4146 [gr-qc].
- [68] M. Pürrer, Frequency domain reduced order model of aligned-spin effective-one-body waveforms with generic mass-ratios and spins, *Phys. Rev. D* **93**, 064041 (2016), arXiv:1512.02248 [gr-qc].
- [69] J. S. Speagle, DYNESTY: a dynamic nested sampling package for estimating Bayesian posteriors and evidences, *Monthly Notices of the Royal Astronomical Society* **493**, 3132 (2020), arXiv:1904.02180 [astro-ph.IM].
- [70] S. Kposov, J. Speagle, K. Barbary, G. Ashton, E. Bennett, J. Buchner, C. Scheffler, B. Cook, C. Talbot, J. Guillochon, P. Cubillos, A. A. Ramos, M. Dartiailh, Ilya, E. Tollerud, D. Lang, B. Johnson, jtmendel, E. Higson, T. Vandal, T. Daylan, R. Angus, patelR, P. Cargile, P. Sheehan, M. Pitkin, M. Kirk, J. Leja, joezuntz, and D. Goldstein, *joshspeagle/dynesty: v2.1.4* (2024).
- [71] LIGO Scientific Collaboration, *Updated Advanced LIGO sensitivity design curve*, Tech. Rep. (2018) <https://dcc.ligo.org/LIGO-T1800044/public>.
- [72] LIGO Scientific Collaboration, *Prospects for Observing and Localizing Gravitational-Wave Transients with Advanced LIGO, Advanced Virgo and KAGRA*, Tech. Rep., <https://dcc.ligo.org/LIGO-P1200087-v42/public>.
- [73] LIGO Scientific Collaboration, *LIGO Algorithm Library - LALSuite*, free software (GPL) (2018).
- [74] L. Pompili, A. Buonanno, H. Estellés, M. Khalil, M. van de Meent, D. P. Mihaylov, S. Ossokine, M. Pürrer, A. Ramos-Buades, A. K. Mehta, R. Cotesta, S. Marsat, M. Boyle, L. E. Kidder, H. P. Pfeiffer, M. A. Scheel, H. R. Rüter, N. Vu, R. Dudi, S. Ma, K. Mitman, D. Melchor, S. Thomas, and J. Sanchez, Laying the foundation of the effective-one-body waveform models seobnr5: Improved accuracy and efficiency for spinning nonprecessing binary black holes, *Phys. Rev. D* **108**, 124035 (2023).
- [75] B. P. Abbott *et al.* (LIGO Scientific, Virgo), Observation of Gravitational Waves from a Binary Black Hole Merger, *Phys. Rev. Lett.* **116**, 061102 (2016), arXiv:1602.03837 [gr-qc].